applied sciences

MDPI

Article

CNN-Assisted Reconstruction of Non-Uniform Temperature Profiles Using Reflected Spectra of a Single Fiber Bragg Grating

Sohyeon Joo and Kyoung Joon Kim *

Department of Mechanical Design Engineering, Pukyong National University, Busan 48513, Republic of Korea; joosohyeon@pukyong.ac.kr
* Correspondence: kjkim@pknu.ac.kr

Abstract

Under non-uniform temperature conditions, the reflected spectrum of a fiber Bragg grating (FBG) can broaden and distort, making a single Bragg wavelength insufficient to describe the axial temperature distribution. This study investigates a one-dimensional convolutional neural network (1D-CNN) for reconstructing non-uniform temperature profiles from the full reflected spectra of a single uniform FBG. A numerical dataset of 2000 paired spectra and temperature profiles was generated using the transfer matrix method (TMM), which relates forward- and backward-propagating optical field amplitudes across grating segments. Four representative profiles—linear, exponential, hyperbolic, and Gaussian—were considered to represent typical temperature distributions associated with heat conduction and localized heating. The CNN was trained to map the 1001-point normalized reflectivity spectrum to a 200-point axial temperature profile. Across five independent training runs, the CNN achieved a mean absolute percentage error (MAPE) of 11.02 ± 0.60%, a root mean square error (RMSE) of 3.06 ± 0.38 K, and a coefficient of determination (R^2) of 0.971 ± 0.005 on the independent test set. Partial least squares (PLS) regression yielded a higher RMSE of 4.08 K. TMM-based iterative optimization reproduced the target profile with errors close to numerical precision but required 28.50 s per spectrum, compared with 6.85 ms for the CNN. Under simulated Gaussian intensity noise, the RMSE of a fixed CNN increased to 4.89 K at 30 dB and 10.73 K at 20 dB, whereas wavelength jitter with a standard deviation of 5 pm yielded an RMSE of 2.76 K. These results suggest that the proposed CNN can reduce online reconstruction time for the investigated temperature profiles, although experimental validation remains necessary.

Keywords: fiber Bragg grating; non-uniform temperature; convolutional neural network; temperature reconstruction

Check for updates

Academic Editor: John Xiupu Zhang

Received: 7 September 2026
Revised: 16 October 2026
Accepted: 2 November 2026
Published: 6 November 2026

Copyright: © 2026 by the authors. Licensee MDPI, Basel, Switzerland. This article is an open access article distributed under the terms and conditions of the Creative Commons Attribution (CC BY) license.

1. Introduction

Fiber Bragg gratings (FBGs) have been widely used as optical filters and sensors for measuring temperature, strain, pressure, and vibration [1–3]. In FBG temperature sensing, changes in the effective refractive index and grating period caused by the thermo-optic effect and thermal expansion shift the Bragg wavelength [2–4]. FBG sensors offer several advantages, including small size, immunity to electromagnetic interference, and remote sensing capability [3,5,6]. However, temperature fields are often spatially non-uniform in engineering applications, such as thermal ablation and battery thermal management [7,8]. Under a uniform temperature change, the reflected spectrum mainly shifts along the wavelength axis while maintaining a similar spectral shape. In contrast, a non-uniform temperature

distribution can cause spectral broadening and distortion because the local Bragg condition varies along the grating [2,9]. Therefore, a single Bragg wavelength cannot fully represent the axial temperature distribution.

Several optical fiber sensing approaches have been developed to obtain spatial temperature information. Arrays of short FBGs provide quasi-distributed temperature measurements, with spatial sampling determined by their length and spacing. Bianchi et al. [7] used FBG arrays for temperature monitoring and feedback control during laser ablation. Sun et al. [10] demonstrated distributed temperature sensing using phase-shifted FBGs interrogated by optical frequency domain reflectometry (OFDR). Zhu et al. [8] reconstructed the surface temperature field of a lithium-ion battery using distributed Rayleigh-scattering measurements. Chirped FBGs provide another approach by introducing a position-dependent grating period [11]. Korganbayev et al. [12] reconstructed temperature profiles from chirped FBG spectra using an iterative model-based method. More recently, Wang et al. [13] employed a neural network to reconstruct temperature distributions using a femtosecond-laser-inscribed chirped FBG for subsurface temperature monitoring during laser-powder bed fusion. These approaches obtain spatial information through multiple sensing locations, distributed optical measurements, or deliberately varied grating periods.

For a conventional uniform FBG, temperature is commonly estimated from a characteristic wavelength of the reflected spectrum. Peak and centroid tracking methods estimate the wavelength shift but do not directly provide the axial temperature distribution [14]. Cięszczyk et al. [15] introduced cumulative sum preprocessing to improve wavelength shift estimation under noisy conditions. Model-based inverse reconstruction provides another means of extracting information from the reflected spectrum. The transfer matrix method (TMM) can describe the spectral response of an FBG under non-uniform conditions [2,9]. Kim et al. applied the TMM to thermo-optical modeling of polymer FBGs under LED illumination [16] and intrinsic heating [17]. Detka and Kaczmarek [18] combined the TMM with Nelder–Mead optimization to reconstruct a non-smooth strain distribution and a temperature value from the reflected intensity spectrum of a uniform FBG. However, iterative reconstruction requires repeated spectral calculations, increasing the computational cost.

Machine learning has also been applied to FBG signal processing to extract information from complex reflection spectra. Djurhuus et al. [19] employed Gaussian process regression for temperature estimation. Kokhanovskiy et al. [20] used deep neural networks to process distorted spectra from a densely inscribed FBG array and estimate the positions of reference reflection peaks for spatial temperature measurement. Cao et al. [21] demonstrated direct temperature demodulation from experimental FBG spectra using a deep convolutional neural network (CNN). Shao et al. [22] combined long short-term memory and convolutional neural networks for temperature estimation, while Tang et al. [23] employed a multi-task one-dimensional CNN for spectral distortion recognition and temperature demodulation. These studies demonstrate the capability of machine learning to extract temperature-related information from reflected spectra. However, most of these methods estimate temperature values or grating-specific spectral features rather than a continuous axial temperature profile within a single FBG.

Despite these developments, reconstructing an axial temperature profile from the full reflected spectrum of a single uniform FBG remains a challenging inverse problem. Different temperature distributions may produce similar spectral responses. Therefore, reconstruction accuracy, computational cost, and sensitivity to spectral perturbations should be evaluated within a clearly defined range of temperature profiles. The objective of the present study is to investigate a one-dimensional convolutional neural network (1D-CNN)-assisted approach for reconstructing non-uniform axial temperature profiles from the full reflected spectra of a single uniform silica FBG. Four temperature-profile shapes—linear,

exponential, hyperbolic, and Gaussian—were selected to represent typical temperature distributions associated with heat conduction and localized heating. A numerical dataset was generated using the TMM, and the CNN was trained to predict the corresponding axial temperature profiles. The reconstruction accuracy and computational cost were compared with those of TMM-based parametric inverse optimization and partial least squares (PLS) regression. Additional numerical tests were conducted to examine the sensitivity of the trained CNN to simulated Gaussian intensity noise and wavelength jitter. The evaluation was restricted to the selected profile shapes and numerical conditions.

2. Theoretical Background

2.1. FBG Temperature Sensing Principle

An FBG is an optical fiber device in which the refractive index of the fiber core is periodically modulated along the axial direction [1–4]. When broadband light is incident on an FBG, a narrow wavelength band satisfying the Bragg condition is reflected, while the remaining wavelengths are transmitted. The Bragg wavelength is determined by the effective refractive index and the grating period as follows [2,4]:

$$\lambda_B = 2n_{eff}\Lambda \tag{1}$$

where λ_B is the Bragg wavelength, n_{eff} is the effective refractive index of the guided mode, and Λ is the grating period. Equation (1) indicates that changes in either the effective refractive index or the grating period shift the Bragg wavelength. Figure 1 illustrates the FBG sensing principle under uniform and non-uniform temperature conditions.

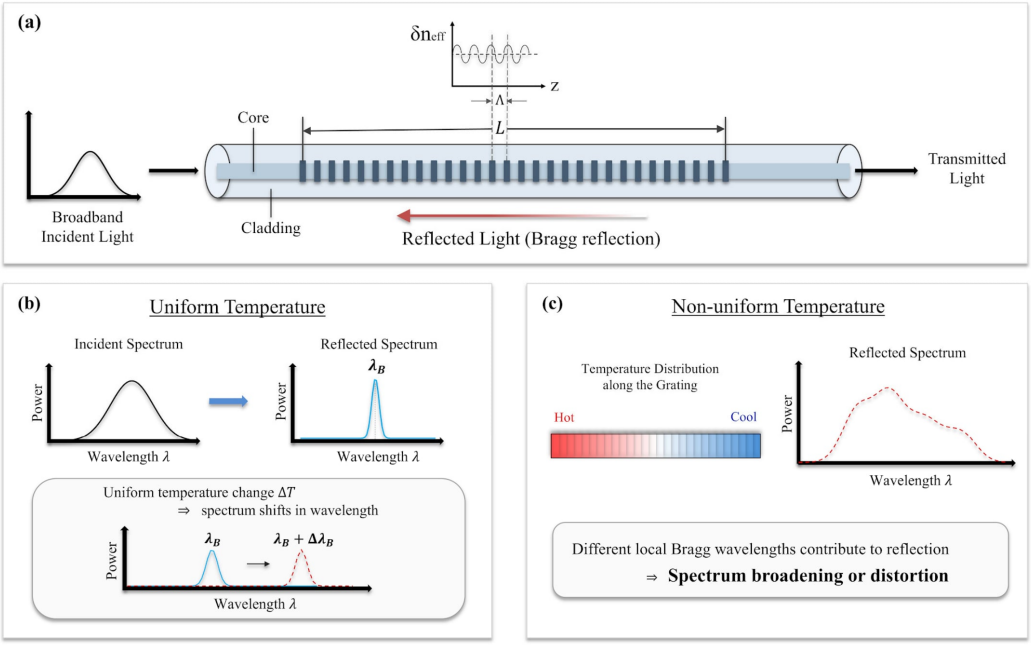


Figure 1. FBG sensing principle: (**a**) Basic structure and reflection mechanism, (**b**) Bragg wavelength shift under uniform temperature, and (**c**) spectral distortion under non-uniform temperature.

Temperature changes affect the effective refractive index through the thermo-optic effect and the grating period through thermal expansion. For a mechanically unconstrained FBG under a uniform temperature change, the normalized Bragg wavelength shift can be expressed as [4,24]:

$$\frac{\Delta\lambda_B}{\lambda_B} = \left(\frac{1}{n_{eff}}\frac{dn}{dT} + \alpha\right)\Delta T \tag{2}$$

where $\Delta\lambda_B$ is the Bragg wavelength shift, dn/dT is the thermo-optic coefficient, α is the thermal expansion coefficient, and ΔT is the temperature change from the reference temperature. Under this condition, the reflected spectrum mainly shifts along the wavelength axis while maintaining a similar spectral shape as shown in Figure 1b.

Under a non-uniform temperature distribution, the effective refractive index and grating period vary along the grating, producing different local Bragg conditions. Consequently, the reflected spectrum can broaden or become distorted, as shown in Figure 1c [2,9]. Equation (2) describes the response to a uniform temperature change, whereas the full reflected spectrum is used to analyze non-uniform temperature profiles.

2.2. Transfer Matrix Method

The transfer matrix method (TMM) was used as the forward optical model to calculate the reflectivity spectrum of a silica FBG under a prescribed axial temperature profile [2]. Silica was considered because of its established use in optical fiber sensing and well-characterized thermo-optic properties [24]. Optical self-heating caused by the interrogating light was neglected under an assumed low-power interrogation condition [25]. Therefore, the axial temperature profile was prescribed independently of the interrogating light. The fiber was assumed to be mechanically unconstrained, without externally applied strain or strain transfer from surrounding structures [26]. Free thermal expansion was retained, whereas polarization-dependent effects were neglected.

In the TMM, the grating is divided into M segments of length $\Delta z = L/M$, where L is the total grating length. Each segment was treated as locally uniform, allowing the forward- and backward-propagating optical fields at adjacent segment boundaries to be related through a transfer matrix [2]. Figure 2 shows the segmented FBG used for the TMM.

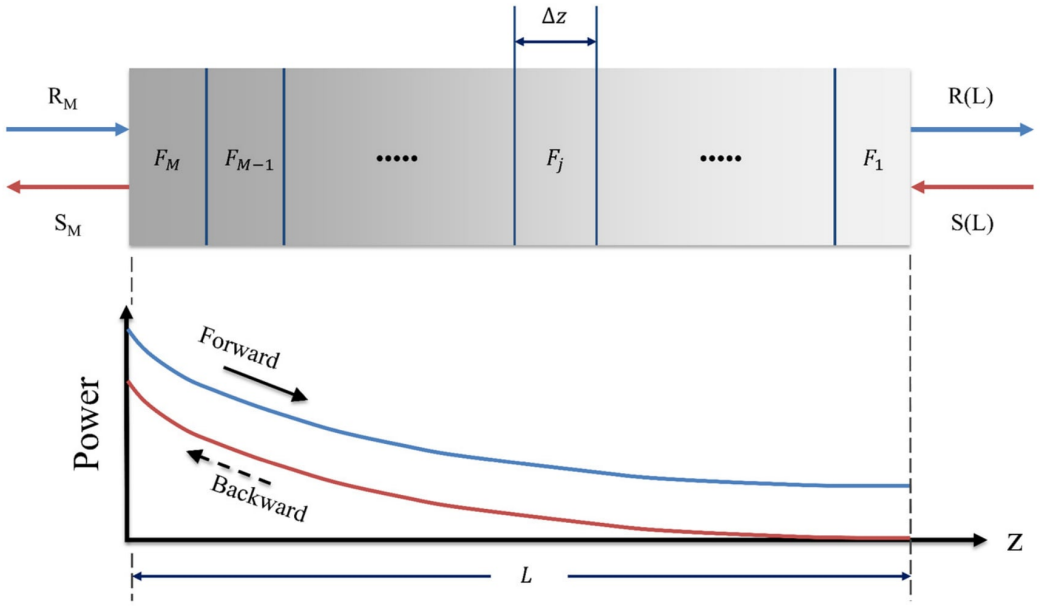


Figure 2. Schematic of the TMM for a segmented FBG and its propagating wave power.

The amplitudes of the forward- and backward-propagating waves are denoted by $R(z)$ and $S(z)$, respectively. For the j-th segment, the coupled-mode equations can be written as [2,27]:

$$\frac{dR}{dz} = -i\hat{\sigma}_j R(z) - i\kappa S(z) \quad (3)$$

$$\frac{dS}{dz} = i\hat{\sigma}_j S(z) + i\kappa R(z) \quad (4)$$

where κ is the coupling coefficient and $\hat{\sigma}_j$ is the "dc" self-coupling coefficient of the j-th segment. Here, $\mathrm{i} = \sqrt{-1}$ is the imaginary unit. Since the optical properties are assumed to be constant within each segment, the solution of Equations (3) and (4) over Δz can be expressed in matrix form as:

$$\begin{bmatrix} R_j(\lambda) \\ S_j(\lambda) \end{bmatrix} = F_j(\lambda) \begin{bmatrix} R_{j-1}(\lambda) \\ S_{j-1}(\lambda) \end{bmatrix} \tag{5}$$

where $F_j(\lambda)$ is the transfer matrix of the j-th segment. The total transfer matrix of the grating is then obtained by multiplying the individual matrices as follows:

$$\begin{bmatrix} R_M(\lambda) \\ S_M(\lambda) \end{bmatrix} = F(\lambda) \begin{bmatrix} R(L) \\ S(L) \end{bmatrix} \tag{6}$$

$$F(\lambda) = F_M(\lambda) F_{M-1}(\lambda) \ldots F_j(\lambda) \ldots F_1(\lambda) \tag{7}$$

In the indexing shown in Figure 2, the segments are numbered from the output end toward the incident end.

For a prescribed local excess temperature θ_j, the effective refractive index and the grating period of the j-th segment are modified as [4,24]:

$$n_{eff,j} = n_{eff,0} + \frac{dn}{dT}\theta_j \tag{8}$$

$$\Lambda_j = \Lambda_0\left(1 + \alpha\theta_j\right) \tag{9}$$

where $n_{eff,0}$ and Λ_0 are the effective refractive index and grating period at the reference temperature, respectively. The detuning value of the j-th segment is then expressed as:

$$\delta_j(\lambda) = \frac{2\pi n_{eff,j}}{\lambda} - \frac{\pi}{\Lambda_j} \tag{10}$$

The "dc" self-coupling coefficient is related to the detuning value and intrinsic attenuation coefficient as:

$$\hat{\sigma}_j(\lambda) = \delta_j(\lambda) - \mathrm{i}\frac{\hat{\alpha}}{2} \tag{11}$$

where $\hat{\alpha}$ is the intrinsic attenuation coefficient. Because optical attenuation in silica fiber is low near 1550 nm, the propagation loss over the 10 mm grating was assumed to be negligible as $\hat{\alpha} = 0$. The coupling coefficient is given by

$$\kappa(\lambda) = \frac{\pi\Delta n}{\lambda} \tag{12}$$

where Δn is the refractive index modulation amplitude of the grating. The eigenvalue of the coupled-mode equations for the j-th segment is defined as:

$$m_j(\lambda) = \sqrt{\kappa^2(\lambda) - \hat{\sigma}_j^2(\lambda)} \tag{13}$$

Using these parameters, the transfer matrix of the j-th segment is written as [2,28]:

$$F_j(\lambda) = \begin{bmatrix} cosh\left(m_j\Delta z\right) - i\frac{\hat{\sigma}_j}{m_j}sinh\left(m_j\Delta z\right) & -i\frac{\kappa}{m_j}sinh\left(m_j\Delta z\right) \\ i\frac{\kappa}{m_j}sinh\left(m_j\Delta z\right) & cosh\left(m_j\Delta z\right) + i\frac{\hat{\sigma}_j}{m_j}sinh\left(m_j\Delta z\right) \end{bmatrix} \tag{14}$$

The boundary condition $R(L) = 1$ and $S(L) = 0$ is applied at the end of the grating, where no backward propagating wave is assumed to be incident from the output side. After the total transfer matrix is obtained, the reflectivity spectrum is calculated as:

$$\rho(\lambda) = \frac{|S_M(\lambda)|^2}{|R_M(\lambda)|^2} \tag{15}$$

Thus, the TMM provides the forward mapping from a prescribed axial temperature profile to the corresponding reflectivity spectrum. Table 1 summarizes the optical, material, and numerical parameters used in the TMM calculations.

Table 1. Parameters used in the TMM calculation.

Parameter	Symbol	Value
(a) Basic parameters		
Radius of core	r_{co}	4.1 μm
Grating length	L	10 mm
Grating period	Λ	532 nm
Refractive index of core	n_{co}	1.46
Numerical aperture	NA	0.14
Bragg wavelength	λ_B	1550 nm
Maximum reflectivity	ρ_{max}	0.8
(b) Derived parameters		
Effective refractive index	n_{eff}	1.4568
Coupling coefficient at λ_B	κ_B	144.36 m^{-1}
Index modulation	Δn	7.12×10^{-5}
(c) Material properties of optical fiber		
Thermo-optical coefficient	dn/dT	8.6×10^{-6} K^{-1}
Coefficient of thermal expansion	α	0.55×10^{-6} K^{-1}
(d) Numerical settings		
Number of axial segments	$M(=N_z)$	200
Number of wavelength points	N_λ	1001
Wavelength range	$\lambda_{min} - \lambda_{max}$	1548–1552 nm

Note: The values in (a)–(c) were adopted from [13] as representative silica FBG parameters, whereas the numerical settings in (d) were specified in the present study.

The grating was divided into $M = 200$ segments so that each segment could be approximated as locally uniform while its length remained sufficiently larger than the grating period, consistent with the piecewise-uniform assumption of the TMM [28]. The reflectivity spectrum was calculated over 1548–1552 nm using $N_\lambda = 1001$ equally spaced wavelength points. This wavelength grid also defines the CNN input dimension.

3. Proposed Method

3.1. Overall Procedure

The overall procedure of the proposed CNN-assisted fiber Bragg grating sensing approach is shown in Figure 3. The procedure consists of two main stages: TMM-based dataset generation and CNN training and evaluation.

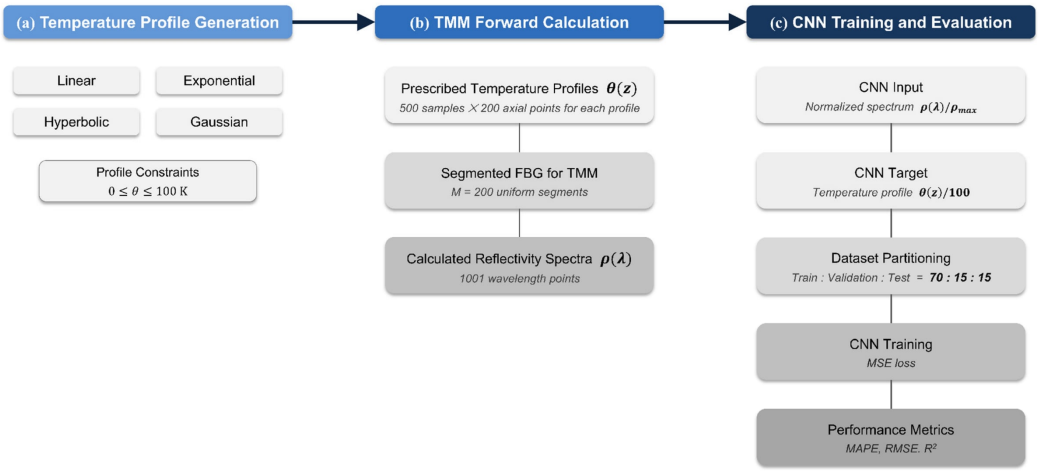


Figure 3. Flowchart of the overall procedure for the proposed CNN-assisted temperature sensing method: (**a**) Temperature profile generation, (**b**) TMM forward calculation, and (**c**) CNN training and evaluation.

In the first stage, four representative non-uniform temperature profiles—linear, exponential, hyperbolic, and Gaussian—were generated along the grating. Each temperature profile was discretized into 200 axial points corresponding to the TMM segments. The local effective refractive index and grating period were then modified based on the local temperature, and the reflectivity spectrum was calculated using the TMM described in Section 2.2. The calculated reflectivity spectrum is paired with the corresponding synthetic temperature profile to construct the numerical dataset.

In the second stage, the generated dataset was divided into training, validation, and test sets. The normalized reflectivity spectra were used as the CNN inputs, and the corresponding normalized axial temperature profiles were used as the target outputs. The training set was used to train the CNN, the validation set was used for hyperparameter selection, and the independent test set was used for final performance evaluation. Once trained, the CNN model can predict an axial temperature profile from a reflected spectrum through a single feed-forward calculation without iterative inverse reconstruction.

3.2. TMM-Generated Dataset

A numerical dataset of paired reflectivity spectra and temperature profiles was generated using the TMM described in Section 2.2. The calculated reflectivity spectra were used as the CNN inputs, and the prescribed temperature profiles were used as the target outputs.

The excess temperature profile is expressed as

$$\theta(z) = T(z) - T_{ref} \tag{16}$$

where θ is the excess temperature, T is the temperature, z is the axial coordinate along the grating, and T_{ref} is the reference temperature. Four representative temperature profile shapes were selected: linear, exponential, hyperbolic, and Gaussian. These profiles were chosen to represent temperature distributions that can arise under typical heat conduction and localized heating conditions. The linear profile corresponds to one-dimensional steady conduction with constant thermal conductivity and no internal heat generation or lateral heat loss [29]. The exponential and hyperbolic profiles are motivated by fin-type conduction with lateral convective heat loss in long and finite domains, respectively [29]. The Gaussian profile provides an idealized representation of a localized hot spot, consistent with Gaussian temperature profiles observed during FBG-base laser ablation monitoring [7].

The linear profile with a monotonic gradient Is defined as:

$$\theta(z) = \theta_0 + (\theta_L - \theta_0)\frac{z}{L} \tag{17}$$

where the two boundary values represent the excess temperatures at the ends of the grating, respectively. The exponential profile with a monotonic nonlinear decay is expressed as:

$$\theta(z) = \theta_0 exp(-\beta z) \tag{18}$$

where β is the decay coefficient. The hyperbolic profile is defined as:

$$\theta(z) = \theta_0 \frac{sinh[\beta(L-z)]}{sinh(\beta L)} + \theta_L \frac{sinh(\beta z)}{sinh(\beta L)} \tag{19}$$

where β controls the nonlinear variation along the grating. The Gaussian representing a localized hot spot is defined as:

$$\theta(z) = \theta_{base} + \theta_p exp\left[-\frac{(z-z_c)^2}{2\sigma^2}\right] \tag{20}$$

where θ_{base} is the baseline excess temperature, θ_p is the peak amplitude, z_c is the center position, and σ is the width parameter. For all the profiles, the excess temperature was constrained to $0 \leq \theta \leq 100$ K.

For each synthetic temperature profile, the grating was discretized into 200 axial sections, corresponding to the TMM segments. The local effective refractive index, grating period, and detuning value were then modified based on the local excess temperature. The corresponding reflectivity spectrum was calculated using the TMM described in Section 2.2.

The calculated reflectivity spectrum was normalized using the reference maximum reflectivity. The normalized reflectivity is defined as:

$$\tilde{\rho}(\lambda_i) = \frac{\rho(\lambda_i)}{\rho_{max}}, \qquad i = 1, 2, \ldots, N_\lambda \tag{21}$$

where ρ_{max} is the maximum reflectivity, λ_i is the i-th wavelength, N_λ is the total number of sampled wavelengths. Here, ρ_{max} was set to 0.8. The temperature profile was also normalized by the maximum excess temperature as follows:

$$\tilde{\theta}(z_j) = \frac{\theta(z_j)}{\theta_{max}}, \qquad j = 1, 2, \ldots, N_z \tag{22}$$

where θ_{max} is 100 K.

The CNN input vector and target vector are then written as:

$$\mathbb{x} = \left[\tilde{\rho}(\lambda_1), \tilde{\rho}(\lambda_2), \ldots, \tilde{\rho}(\lambda_{N_\lambda})\right]^T \tag{23}$$

$$\mathbb{y} = \left[\tilde{\theta}(z_1), \tilde{\theta}(z_2), \ldots, \tilde{\theta}(z_{N_z})\right]^T \tag{24}$$

where $\mathbb{x}$ and $\mathbb{y}$ represent the normalized reflectivity spectrum and normalized axial temperature profile, respectively.

To obtain a balanced dataset, 500 samples were generated for each profile shape, resulting in 2000. The dataset was divided into training, validation, and test sets with a ratio of 70:15:15. The dataset configuration is summarized in Table 2.

Table 2. Dataset partitioning for the four temperature profile shapes.

Profile Shape	Total Samples	Training	Validation	Test
Linear	500	350	75	75
Exponential	500	350	75	75
Hyperbolic	500	350	75	75
Gaussian	500	350	75	75
Total	2000	1400	300	300

The generated temperature profiles were projected onto the first two principal components to visualize the dataset distribution. The first two principal components accounted for 90.16% of the total variance. As shown in Figure 4, the four profile shapes occupy partially overlapping regions in the PCA space rather than forming completely separated clusters. The PCA projection was used only for visualization and was not used for CNN training or model selection.

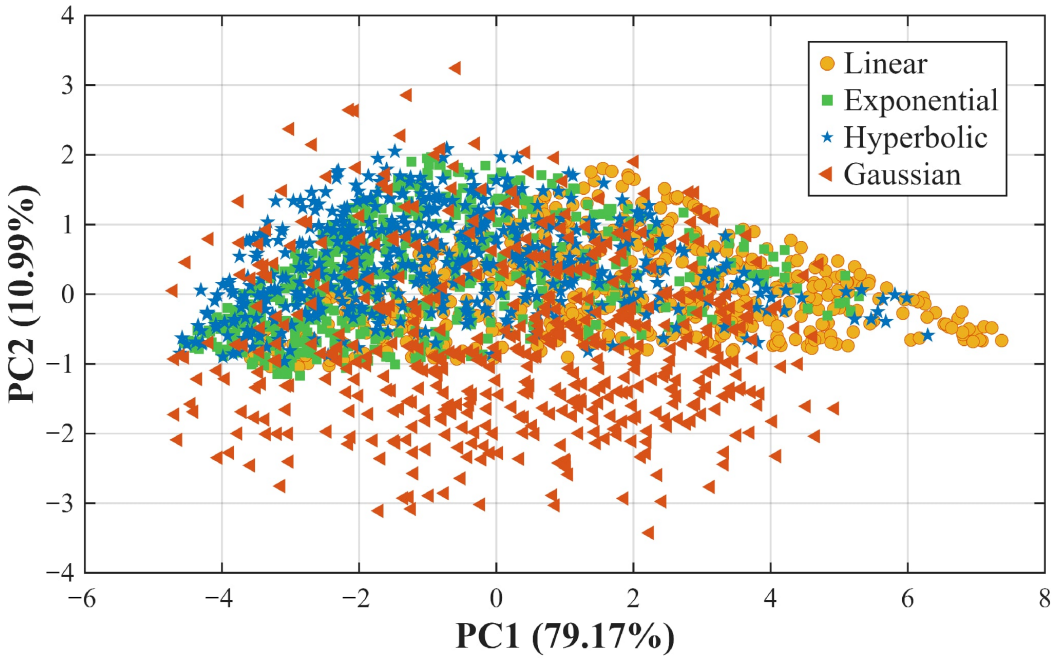


Figure 4. PCA projection of the synthetic temperature profiles onto the 2D feature space.

3.3. CNN Architecture

A one-dimensional convolutional neural network (1D-CNN) was used to predict the axial temperature profile from the reflectivity spectrum. The input to the CNN was a normalized reflectivity spectrum consisting of 1001 wavelength points, and the output was a normalized axial temperature profile consisting of 200 points along the grating.

The reflectivity spectrum contains wavelength-dependent features associated with non-uniform temperature distributions, including peak shifts, spectral broadening, distortion, and sidelobe variations. Therefore, a 1D-CNN was adopted to extract local spectral features from the full reflectivity spectrum.

The CNN architecture is shown in Figure 5. The network consists of two convolutional (Conv) blocks followed by fully connected (FC) layers. Each convolutional layer uses 32 filters with a kernel size of (3, 1), a stride of (1, 1), and same padding. Each convolutional layer is followed by batch normalization and a rectified linear unit (ReLU) activation function. No pooling layer is used. The feature maps after the second convolutional layer are flattened into 32,032 features and passed to a fully connected layer with 256 neurons. Dropout layers are applied after Conv2 and FC1. The final FC layer predicts the normalized temperature profile at 200 axial points. The network contains 8,255,208 trainable parameters. Table 3 summarizes the detailed structure of the proposed 1D-CNN model.

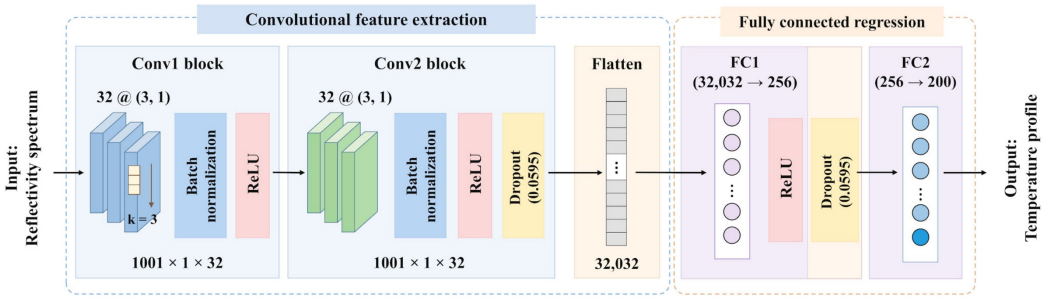


Figure 5. Architecture of the proposed 1D-CNN model for temperature profile prediction.

Table 3. Detailed structure of the proposed 1D-CNN model.

Layer	Type	Filter Size	Stride	Channels
Layer 1	Convolution	(3, 1)	(1, 1)	32
	Batch normalization	–	–	–
	ReLU	–	–	–
Layer 2	Convolution	(3, 1)	(1, 1)	32
	Batch normalization	–	–	–
	ReLU	–	–	–
	Dropout	–	–	–
Regression	Fully connected	–	–	256
	ReLU	–	–	–
	Dropout	–	–	–
	Fully connected	–	–	200

Note: No pooling; same padding; fully connected layers (32,032–256–200). A dash (–) indicates that the corresponding parameter is not applicable or is not separately specified.

The CNN can be regarded as a nonlinear regression model that learns the inverse mapping from the normalized reflectivity spectrum to the normalized temperature profile, expressed as:

$$\hat{y} = f_{CNN}(x) \tag{25}$$

where $\hat{y}$ is the predicted normalized temperature profile, and f_{CNN} represents the trained CNN model. The predicted temperature profile was converted to physical units by multiplying the normalized output by $\theta_{max} = 100$ K. The detailed training settings are described in Section 3.4.

3.4. Training and Evaluation

The CNN model was trained using the numerical dataset generated with the TMM. The independent test dataset was excluded from model training and hyperparameter selection and was used only for the final performance evaluation.

The CNN was trained by minimizing the mean squared error (MSE) loss between the predicted and target normalized temperature profiles. The MSE loss is defined as:

$$\mathcal{L}_{MSE} = \frac{1}{N_z}\sum_{j=1}^{N_z}\left(\tilde{\theta}_j - \hat{\tilde{\theta}}_j\right)^2 \tag{26}$$

where $\tilde{\theta}_j$ is the target normalized excess temperature at the j-th axial point, and $\hat{\tilde{\theta}}_j$ is the corresponding CNN prediction. The Adam optimizer was used for model training. The training and validation losses were monitored to assess convergence.

The main hyperparameters of the CNN model were selected using Bayesian optimization by minimizing the validation RMSE in K. The optimization was performed for 30 objective evaluations, with each candidate model trained for up to 70 epochs. The search ranges and selected hyperparameters are summarized in Table 4. After hyperparameter selection, the final CNN model was trained for 80 epochs using the optimized settings.

Table 4. Bayesian optimization search space and selected hyperparameters.

Hyperparameter	Search Range	Selected Value
Initial learning rate	$5 \times 10^{-5} - 2 \times 10^{-3}$	1.86×10^{-4}
Conv1 filters	[16, 32, 48]	32
Conv2 filters	[32, 64, 96]	32
Kernel size	[3, 5, 7]	3
FC neurons	[128, 256, 512]	256
Dropout rate	0 – 0.25	0.0595
L2 regularization	$10^{-6} - 10^{-3}$	3.45×10^{-5}
Mini-batch size	[16, 32, 64]	16

To assess the variability, the final model was trained five times using random seeds 1–5, while keeping the data partitions, network architecture, and optimized hyperparameters fixed. Bayesian optimization was performed only once, and the test results are reported as the mean ± sample standard deviation (SD) across the five runs.

The prediction performance was evaluated using three metrics: mean absolute percentage error (MAPE), root mean squared error (RMSE), and coefficient of determination (R^2). The predicted normalized temperature profile was first converted to excess temperatures in K before evaluation.

The MAPE is defined as:

$$\mathrm{MAPE} = \frac{1}{N_z} \sum_{j=1}^{N_z} \left| \frac{\theta_j - \hat{\theta}_j}{\theta_j} \right| \times 100 \tag{27}$$

where θ_j and $\hat{\theta}_j$ are the target and predicted excess temperatures at the j-th axial point, respectively. MAPE quantifies the relative prediction error, but it is sensitive to target temperatures near zero. Therefore, RMSE was also used to quantify the prediction error in temperature units. The RMSE is defined as:

$$\mathrm{RMSE} = \sqrt{\frac{1}{N_z} \sum_{j=1}^{N_z} \left(\theta_j - \hat{\theta}_j \right)^2} \tag{28}$$

The R^2 was used to evaluate the agreement between the target and predicted temperature profiles and is defined as:

$$R^2 = 1 - \frac{\sum_{k=1}^{N_s} \sum_{j=1}^{N_z} \left(\theta_{k,j} - \hat{\theta_{k,j}} \right)^2}{\sum_{k=1}^{N_s} \sum_{j=1}^{N_z} \left(\theta_{k,j} - \overline{\theta} \right)^2} \tag{29}$$

where N_s is the number of test samples in the evaluated group, and $\overline{\theta}$ is the mean target temperature using all values in that group. MAPE and RMSE were calculated for each independent test sample over the 200 axial points and then averaged over the corresponding test samples. In contrast, R^2 was calculated globally using all target and predicted temperature values within each profile group or the complete test set.

3.5. Baseline Methods

To provide quantitative baselines for the proposed CNN, two additional reconstruction methods were evaluated: TMM-based parametric inverse optimization and partial least squares (PLS) regression. Both methods were evaluated on the same independent test set of 300 spectra, using the same 200-point axial temperature profiles and performance metrics as the CNN.

For the optimization-based baseline, the temperature profiles were reconstructed by fitting TMM-calculated spectra to the input spectra using the forward model described in Section 2.2. For each input spectrum, the four profile shapes considered in this study were fitted independently using bounded nonlinear least-squares optimization. The profile parameters were constrained to the ranges used for the synthetic dataset generation. A fixed initialization bank containing 128 candidates for each profile shape was generated, and four initial points were used for each shape. The solution producing the minimum full-spectrum residual was selected as the reconstructed profile. Neither the true profile shape nor the target temperature profile was provided to the optimization procedure. TMM-based inverse reconstruction combined with iterative optimization has also been reported in previous studies [18].

PLS regression was also evaluated as a simple data-driven baseline. A single multivariate PLS model was used to map the 1001-point normalized reflectivity spectrum to the 200-point normalized temperature profile. The number of latent components was selected using only the validation set. Components from 1 to 100 were examined, and 56 components were selected based on the minimum validation RMSE. The final PLS model was fitted using the training set, and the independent test set was used only for the final evaluation. PLS was implemented using the SIMPLS formulation [30]. The normalized PLS outputs were converted to excess temperatures in K using the same scaling factor as the CNN.

All computations were implemented in MATLAB R2025a Update 1 (MathWorks, Natick, MA, USA). Reconstruction times were measured on the CPU for individual input spectra, excluding file input/output and performance metric calculations. For the CNN and PLS models, inference time was measured over 100 repeated runs after five warm-up runs. For the iterative optimization method, the reconstruction time was recorded separately for all 300 test spectra. The calculations were performed on a desktop computer equipped with a 13th Gen Intel® Core™ i5-13400 CPU (2.50 GHz), 32 GB of RAM, and an NVIDIA GeForce GT 1030 GPU. CNN training was performed on the GPU, and the training time was recorded separately, excluding test inference and model saving.

4. Results and Discussion

4.1. Training Results

The training behavior of the CNN model was evaluated by monitoring the MSE loss. Figure 6 shows the training and validation MSE curves from a representative training run. Both losses decreased rapidly during the early epochs and gradually stabilized as training progressed. This trend suggests that the CNN converged under the selected training settings in the representative run.

The training and validation curves followed similar trends without pronounced divergence toward the end of training. In particular, the validation loss did not show a sustained increase during the later epochs, suggesting no clear deterioration in validation performance. However, the MSE losses were calculated using normalized temperature profiles and do not directly quantify reconstruction errors in physical units. Furthermore, convergence in a representative run does not establish the prediction accuracy for individual temperature profile shapes. The reconstruction performance was subsequently evaluated using the independent test set, as described in Section 4.2.

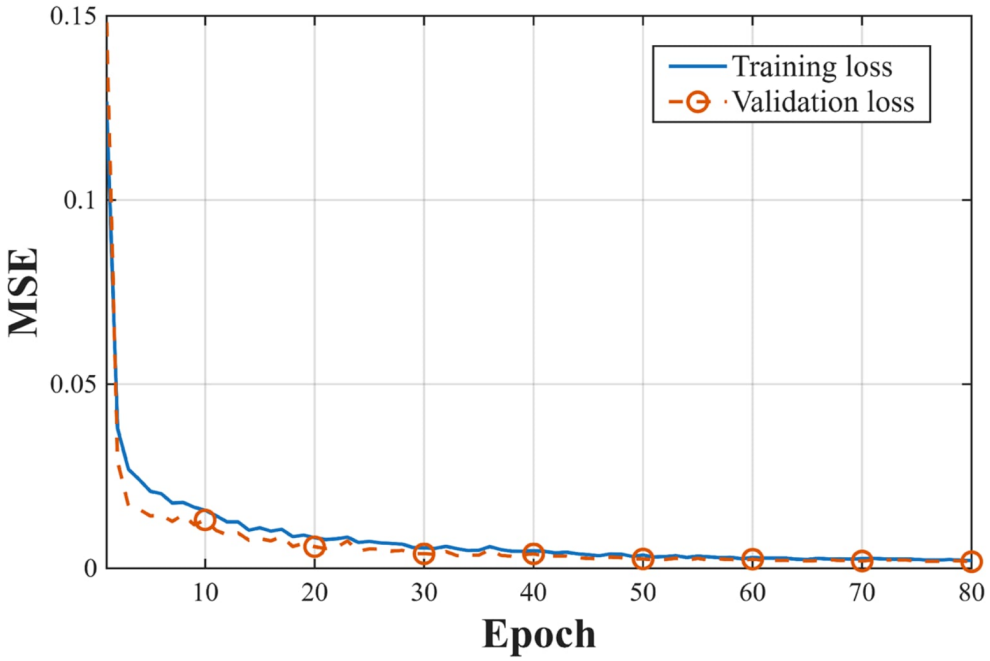


Figure 6. Training and validation loss curves of the proposed 1D-CNN model.

4.2. Model Performance

The reconstruction performance was evaluated using the independent test set of 300 spectra. The CNN was compared with the TMM-based parametric inverse optimization and PLS regression described in Section 3.5. The CNN results are reported as the mean ± standard deviation (SD) across the five training runs, whereas the baseline results correspond to fixed evaluations. The results are summarized in Table 5.

Table 5. Comparison of reconstruction performance on the independent test set.

Profile Shape	Method	MAPE (%)	RMSE (K)	R^2
Linear	CNN	5.49 ± 1.14	2.45 ± 0.60	0.984 ± 0.008
	TMM-based optimization	$< 10^{-8}$	$< 10^{-8}$	1.000
	PLS	7.24	3.00	0.978
Exponential	CNN	8.63 ± 0.90	1.53 ± 0.33	0.993 ± 0.003
	TMM-based optimization	$< 10^{-8}$	$< 10^{-8}$	1.000
	PLS	9.79	2.21	0.987
Hyperbolic	CNN	8.86 ± 0.70	2.37 ± 0.35	0.984 ± 0.004
	TMM-based optimization	$< 10^{-8}$	$< 10^{-8}$	1.000
	PLS	11.32	3.33	0.966
Gaussian	CNN	21.11 ± 1.71	5.91 ± 0.39	0.908 ± 0.009
	TMM-based optimization	$< 10^{-8}$	$< 10^{-8}$	1.000
	PLS	34.67	7.78	0.836
Total	CNN	11.02 ± 0.60	3.06 ± 0.38	0.971 ± 0.005
	TMM-based optimization	$< 10^{-8}$	$< 10^{-8}$	1.000
	PLS	15.76	4.08	0.948

Under the noise-free numerical conditions, the TMM-based optimization reproduced the target profiles with errors close to numerical precision because the same TMM forward model, profile shapes, and parameter ranges were used for both dataset generation and inverse reconstruction. For the complete test set, the CNN achieved a MAPE of 11.02 ± 0.60%, an RMSE of 3.06 ± 0.38 K, and an R^2 of 0.971 ± 0.005. The CNN showed lower MAPE and RMSE values and a higher R^2 than PLS regression, which yielded a MAPE of 15.76%, an RMSE of 4.08 K, and an R^2 of 0.948.

The Gaussian profile showed the largest reconstruction errors for both data-driven methods. Its localized hot spot requires the peak magnitude, position, and width to be reconstructed simultaneously, and small spatial errors can therefore produce relatively large pointwise errors. In addition, the low-temperature regions away from the hot spot can increase MAPE because the target temperature appears in the denominator. Figure 7 shows the sample-wise MAPE distributions for a representative CNN run.

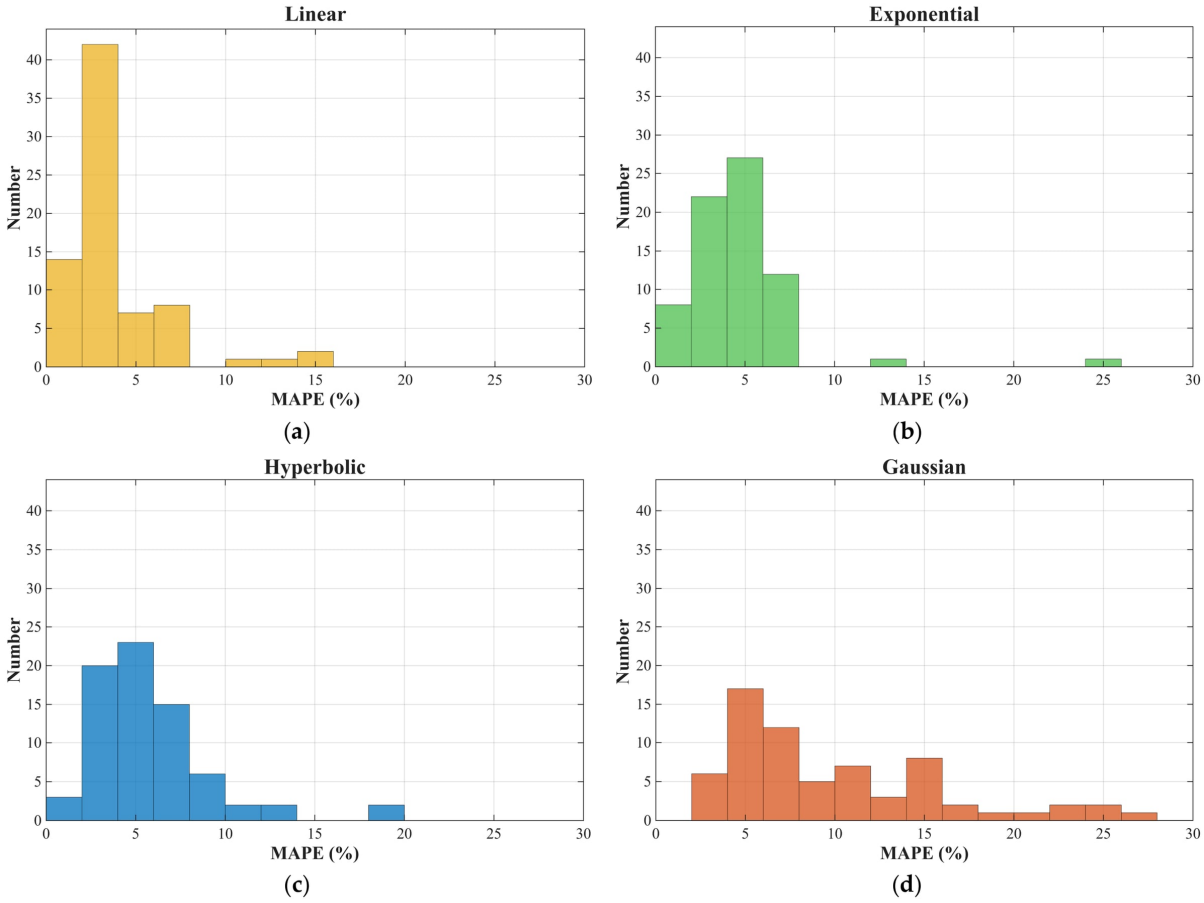


Figure 7. Sample-wise MAPE histograms for different shapes: (**a**) linear, (**b**) exponential, (**c**) hyperbolic, and (**d**) Gaussian.

Representative reconstruction results from the CNN, TMM-based optimization, and PLS regression are compared in Figure 8. The CNN curves correspond to a representative training run. The optimization results nearly overlap the target profiles, while the CNN generally follows the targets more closely than PLS. Larger deviations are observed for both data-driven methods in the Gaussian case, consistent with the results in Table 5.

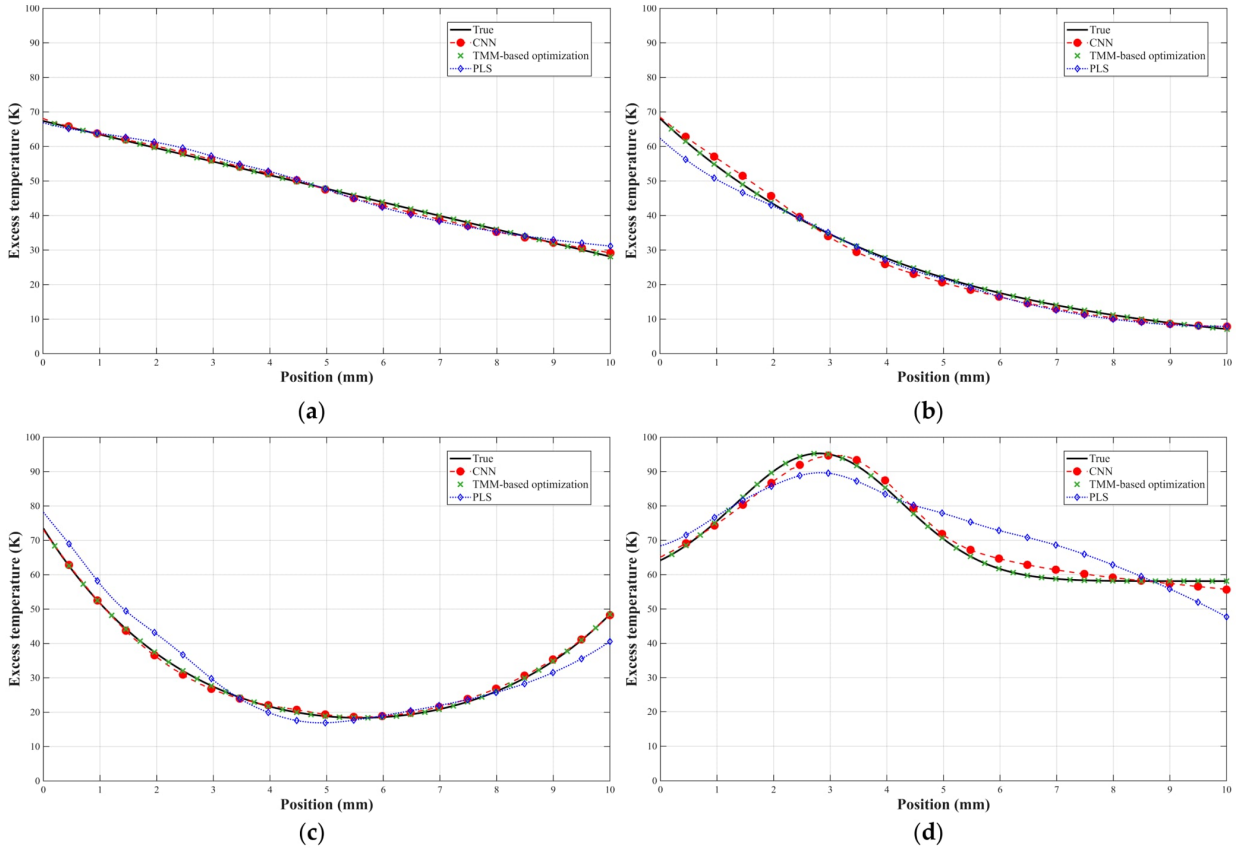


Figure 8. Representative temperature profile reconstructions obtained using the CNN, TMM-based optimization, and PLS regression compared with target profiles: (**a**) linear, (**b**) exponential, (**c**) hyperbolic, and (**d**) Gaussian.

The computational characteristics are summarized in Table 6. The median CPU reconstruction time was 28.50 s per spectrum for the TMM-based optimization and 6.85 ms for the CNN, indicating a reduction of more than three orders of magnitude in online reconstruction time. PLS provided the shortest inference time of 0.0086 ms but showed larger reconstruction errors than the CNN. These results indicate that the CNN provided lower reconstruction errors than PLS while requiring substantially less CPU time than TMM-based iterative optimization. In terms of model complexity, the CNN contained 8,255,208 trainable parameters, whereas the PLS model used 56 latent components. The iterative optimization involved 2–4 profile parameters, depending on the assumed profile shape, but required approximately 1284 TMM evaluations per spectrum on average.

Table 6. Computational characteristics of the reconstruction methods.

Method	Offline Preparation	Median CPU Time per Spectrum
CNN	Training time: 275.7 ± 2.4 s	6.85 ms
TMM-based optimization	Initialization time: 11.29 s	28.50 s
PLS	Component selection and fitting: 43.03 s	0.0086 ms

Note: CNN training time is mean ± SD over five GPU runs. CPU runtimes are medians; CNN/PLS used 100 repeated runs and optimization used 300 test spectra.

These results should be interpreted within the scope of the present numerical model. The nearly exact optimization results do not establish the uniqueness of the inverse reconstruction for arbitrary temperature distributions. In addition, the FBG was assumed to be mechanically unconstrained, so strain transfer associated with bonding, packaging, or embedding was not considered. The CNN was also trained and evaluated only within the four selected profile shapes and parameter ranges. Therefore, its applicability to experimental spectra and temperature distributions outside this domain remains to be established. The sensitivity of the trained CNN to simulated intensity noise and wavelength-axis perturbations is further evaluated in Section 4.3.

4.3. Noise Robustness Evaluation

To evaluate the sensitivity of the proposed CNN to spectral perturbations, additional numerical tests were performed using Gaussian intensity noise and wavelength jitter. A single trained CNN was kept fixed, and the same independent test set of 300 samples was used without retraining.

Gaussian intensity noise was added to the normalized reflectivity spectra at signal-to-noise ratios (SNRs) of 40, 30, and 20 dB, defined as the ratio of the mean squared spectral signal to the mean squared added noise. The noise power was adjusted for each spectrum to satisfy the prescribed SNR without clipping the perturbed inputs. Negri et al. [31] evaluated Gaussian noise over an SNR range of 16–60 dB. Experimental studies have also reported a 30 dB difference between the reflected spectral peak and the background noise level [32] and photocurrent measurement SNRs of 35–42 dB [33]. However, these experimental SNR measures are not directly equivalent to the SNR defined in this study.

Wavelength jitter was simulated by applying an independently sampled Gaussian wavelength offset to each spectrum, with standard deviations of 1, 2, and 5 pm. The shifted spectra were linearly interpolated onto the original wavelength grid. For each perturbation condition, 10 independent realizations were evaluated, and the results are reported as the mean ± standard deviation (SD). MAPE and RMSE were averaged over individual test samples, whereas R^2 was calculated globally over the test set. The noise-free condition was deterministic.

Table 7 summarizes the reconstruction performance under the different perturbation conditions. Under Gaussian intensity noise, the RMSE increased from 2.68 K under noise-free conditions to 3.09 K at 40 dB and 4.89 K at 30 dB. At 30 dB, R^2 remained at 0.944 despite the increased reconstruction error. However, at 20 dB, the RMSE increased to 10.73 K and R^2 decreased to 0.762, indicating considerable performance degradation under stronger intensity noise. In contrast, wavelength jitters produced relatively small changes in reconstruction accuracy over the investigated range. At a jitter standard deviation of 5 pm, the RMSE was 2.76 K and R^2 remained at 0.976.

Table 7. Reconstruction performance of the fixed CNN under simulated Gaussian intensity noise and wavelength jitter.

Perturbation	Condition	MAPE (%)	RMSE (K)	R^2
None	Clean	9.64	2.68	0.9770
Gaussian intensity noise	40 dB	10.51 ± 0.03	3.09 ± 0.01	0.9729 ± 0.0002
	30 dB	15.18 ± 0.12	4.89 ± 0.04	0.9443 ± 0.0011
	20 dB	34.33 ± 0.27	10.73 ± 0.14	0.7624 ± 0.0059
Wavelength jitter	σ = 1 pm	9.63 ± 0.03	2.68 ± 0.01	0.9769 ± 0.0001
	σ = 2 pm	9.65 ± 0.08	2.70 ± 0.01	0.9766 ± 0.0003
	σ = 5 pm	9.92 ± 0.11	2.76 ± 0.02	0.9758 ± 0.0005

These results indicate that the reconstruction accuracy was more sensitive to additive intensity noise than to the investigated wavelength offsets. Nevertheless, the evaluation was limited to simulated perturbations applied to TMM-generated spectra. Experimental validation is therefore required to assess the applicability of the proposed CNN under actual measurement conditions.

5. Conclusions

This study investigated a 1D-CNN-assisted method for reconstructing non-uniform axial temperature profiles from the full reflected spectra of a single uniform silica FBG. A numerical dataset of 2000 paired reflectivity spectra and temperature profiles was generated using TMM. Four representative temperature profiles—linear, exponential, hyperbolic, and Gaussian—were considered. The CNN was trained to predict a 200-point axial excess temperature profile.

Across five independent training runs, the CNN achieved an overall MAPE of $11.02 \pm 0.60\%$, an RMSE of 3.06 ± 0.38 K, and an R^2 of 0.971 ± 0.005 on the independent test set. The Gaussian profiles showed larger reconstruction errors than the other profile shapes, likely due to the difficulty of reconstructing localized hot spots. The CNN provided lower reconstruction errors than PLS regression, which yielded a MAPE of 15.76% and an RMSE of 4.08 K. Under matched noise-free conditions, the TMM-based iterative optimization reproduced the target profiles with errors close to numerical precision. However, its median CPU reconstruction time was 28.50 s per spectrum, compared with 6.85 ms for the CNN.

Additional numerical tests were performed to examine the sensitivity of a fixed trained CNN to simulated intensity noise and wavelength jitter. Under Gaussian intensity noise, the RMSE increased to 4.89 K at 30 dB and 10.73 K at 20 dB. In contrast, wavelength jitter with a standard deviation of 5 pm resulted in an RMSE of 2.76 K, indicating relatively small changes in reconstruction accuracy over the investigated jitter range.

These findings suggest that the proposed CNN can provide a computationally efficient alternative to TMM-based iterative optimization for the investigated temperature profile shapes. However, the results were obtained using TMM-generated spectra under controlled numerical conditions. Mechanical strain transfer and actual measurement conditions were not considered in the numerical model. Further experimental validation and evaluation of temperature distributions outside the training domain are required to establish the applicability of the proposed method.

Author Contributions: Conceptualization, K.J.K.; methodology, S.J. and K.J.K.; formal analysis, S.J.; investigation, S.J.; data curation, S.J.; writing—original draft preparation, S.J. and K.J.K.; writing—review and editing, K.J.K.; visualization, S.J.; supervision, K.J.K. All authors have read and agreed to the published version of the manuscript.

Funding: This research was supported by the Regional Innovation System & Education (RISE) program through the institute for Regional Innovation System & Education in Busan Metropolitan City, funded by the Ministry of Education (MOE) and the Busan Metropolitan City, Republic of Korea. (2026-RISE(ANCHOR)-02-001-002). This work was supported by the Global Joint Research Program funded by the Pukyong National University (202505850001).

Institutional Review Board Statement: Not applicable.

Informed Consent Statement: Not applicable.

Data Availability Statement: The raw data supporting the conclusions of this article will be made available by the authors on request.

Conflicts of Interest: The authors declare no conflicts of interest.

Nomenclature

Roman symbols	
dn/dT	Thermo-optic coefficient [K^{-1}]
F, F_j	Total and segment transfer matrices
f_{CNN}	Trained CNN model
L	Total grating length [mm]
$m_j(\lambda)$	Eigenvalue of the coupled-mode equations for the j-th segment [m^{-1}]
M	Number of axial segments
n_{eff}	Effective refractive index of the guided mode
$n_{eff,0}$	Effective refractive index at the reference temperature
N_λ	Total number of wavelengths used for TMM
N_s	Number of test samples in the evaluated group
N_z	Number of axial points
$R(z)$, $S(z)$	Forward- and backward-propagating optical field amplitudes
$T(z)$	Temperature [K]
T_{ref}	Reference temperature [K]
$\mathbb{x}$	Normalized reflectivity spectrum
$\mathbb{y}$	Normalized axial temperature profile
$\hat{\mathbb{y}}$	Predicted normalized temperature profile
z	Axial coordinate along the grating [mm]
Greek symbols	
α	Thermal expansion coefficient [K^{-1}]
$\hat{\alpha}$	Intrinsic attenuation coefficient [m^{-1}]
Δn	Refractive index modulation amplitude of the grating
Δz	Segment length [mm]
$\delta_j(\lambda)$	Detuning value of the j-th segment [m^{-1}]
$\kappa(\lambda)$	Coupling coefficient [m^{-1}]
κ_B	Coupling coefficient at λ_B[m^{-1}]
λ	Wavelength [nm]
λ_B	Bragg wavelength [nm]
Λ	Grating period [nm]
Λ_0	Grating period at the reference temperature [nm]
$\rho(\lambda)$	Reflectivity spectrum
ρ_{max}	Reference maximum reflectivity
$\tilde{\rho}(\lambda_i)$	Normalized reflectivity
$\hat{\sigma}_j(\lambda)$	"dc" self-coupling coefficient of the j-th segment [m^{-1}]
$\theta(z)$	Excess temperature [K]
θ_j	Local excess temperature [K]
θ_{max}	Maximum excess temperature [K]
$\tilde{\theta}(z_j)$	Normalized excess temperature
$\hat{\tilde{\theta}}_j$	Corresponding CNN prediction
$\hat{\theta}_j$	Predicted excess temperature at the j-th axial point [K]
$\underline{\theta}$	Mean value of the target temperature profile [K]

References

1. Hill, K.O.; Meltz, G. Fiber Bragg grating technology fundamentals and overview. *J. Light. Technol.* **1997**, *15*, 1263–1276. [CrossRef]
2. Erdogan, T. Fiber grating spectra. *J. Light. Technol.* **1997**, *15*, 1277–1294. [CrossRef]
3. Kersey, A.D.; Davis, M.A.; Patrick, H.J.; LeBlanc, M.; Koo, K.P. Fiber grating sensors. *J. Light. Technol.* **1997**, *15*, 1442–1463. [CrossRef]
4. Kashyap, R. *Fiber Bragg Gratings*; Academic Press: San Diego, CA, USA, 1999.
5. Mihailov, S.J. Fiber Bragg grating sensors for harsh environments. *Sensors* **2012**, *12*, 1898–1918. [CrossRef]

6. Zaynetdinov, M.; See, E.M.; Geist, B.; Ciovati, G.; Robinson, H.D.; Kochergin, V. A fiber Bragg grating temperature sensor for 2–400 K. *IEEE Sens. J.* **2015**, *15*, 1908–1912. [CrossRef]
7. Bianchi, L.; Korganbayev, S.; Orrico, A.; De Landro, M.; Saccomandi, P. Quasi-distributed fiber optic sensor-based control system for interstitial laser ablation of tissue: Theoretical and experimental investigations. *Biomed. Opt. Express* **2021**, *12*, 2841–2858. [CrossRef]
8. Zhu, Y.; Zhang, X.; Shang, Y.; Yu, M.; Gu, X.; Li, J.; Hou, L. Utilized distributed optical fiber sensor with spiral-serpentine deployment enabling high-precision full-field temperature reconstruction and thermal management for pouch lithium-ion battery. *Adv. Sci.* **2025**, *12*, e11030. [CrossRef]
9. Gassino, R.; Perrone, G.; Vallan, A. Temperature monitoring with fiber Bragg grating sensors in nonuniform conditions. *IEEE Trans. Instrum. Meas.* **2020**, *69*, 1336–1343. [CrossRef]
10. Sun, Z.; Xiao, X.; Zhao, W.; Ai, K.; Lv, Y.; Liu, H.; Sun, Q.; Yan, Z. High-precision distributed temperature sensor based on phase-shifted FBGs interrogated by OFDR. *J. Light. Technol.* **2025**, *43*, 2357–2362. [CrossRef]
11. Won, P.C.; Leng, J.; Williams, J.A.R. Distributed temperature sensing using a chirped fibre Bragg grating. *Meas. Sci. Technol.* **2004**, *15*, 1501–1505. [CrossRef]
12. Korganbayev, S.; Orazayev, Y.; Sovetov, S.; Bazyl, A.; Schena, E.; Massaroni, C.; Gassino, R.; Vallan, A.; Perrone, G.; Saccomandi, P.; et al. Detection of thermal gradients through fiber-optic chirped fiber Bragg grating (CFBG): Medical thermal ablation scenario. *Opt. Fiber Technol.* **2018**, *41*, 48–55. [CrossRef]
13. Wang, R.; Wang, R.; Dou, C.; Yang, S.; Gnanasambandam, R.; Wang, A.; Kong, Z. Sub-surface thermal measurement in additive manufacturing via machine learning-enabled high-resolution fiber optic sensing. *Nat. Commun.* **2024**, *15*, 7568. [CrossRef]
14. Tosi, D. Review and analysis of peak tracking techniques for fiber Bragg grating sensors. *Sensors* **2017**, *17*, 2368. [CrossRef]
15. Cięszczyk, S.; Kida, M.; Panas, P. Demodulation of fibre Bragg grating sensors by using cumulative sum as a preprocessing method. *Sensors* **2025**, *25*, 634. [CrossRef]
16. Kim, K.J.; Bar-Cohen, A.; Han, B. Thermo-optical modeling of polymer fiber Bragg grating illuminated by light emitting diode. *Int. J. Heat Mass Transf.* **2007**, *50*, 5241–5248. [CrossRef]
17. Kim, K.J.; Bar-Cohen, A.; Han, B. Thermo-optical modeling of an intrinsically heated polymer fiber Bragg grating. *Appl. Opt.* **2007**, *46*, 4357–4370. [CrossRef]
18. Detka, M.; Kaczmarek, C. Simultaneous restoration of a non-smooth strain distribution and temperature of an optical fiber Bragg grating based on its intensity spectrum. *Infrared Phys. Technol.* **2025**, *145*, 105738. [CrossRef]
19. Djurhuus, M.S.E.; Werzinger, S.; Schmauss, B.; Clausen, A.T.; Zibar, D. Machine learning assisted fiber Bragg grating-based temperature sensing. *IEEE Photonics Technol. Lett.* **2019**, *31*, 939–942. [CrossRef]
20. Kokhanovskiy, A.; Shabalov, N.; Dostovalov, A.; Wolf, A. Highly dense FBG temperature sensor assisted with deep learning algorithms. *Sensors* **2021**, *21*, 6188. [CrossRef]
21. Cao, Z.; Zhang, S.; Xia, T.; Liu, Z.; Li, Z. Spectral demodulation of fiber Bragg grating sensor based on deep convolutional neural networks. *J. Light. Technol.* **2022**, *40*, 4429–4435. [CrossRef]
22. Shao, X.; Chang, S.; Zhao, Y.; Jiang, H. Temperature prediction based on long short-term memory convolutional neural network Bragg grating sensing. *Microw. Opt. Technol. Lett.* **2024**, *66*, e34214. [CrossRef]
23. Tang, R.; Jiang, H.; Cao, Z. Parallel processing of FBG spectral distortion recognition and temperature demodulation based on multi-task learning. *Opt. Commun.* **2025**, *578*, 131505. [CrossRef]
24. Rego, G.M. Temperature dependence of the thermo-optic coefficient of GeO_2-doped silica glass fiber. *Sensors* **2024**, *24*, 4857. [CrossRef]
25. Arora, A.; Esmaeelpour, M.; Bernier, M.; Digonnet, M.J.F. High-resolution slow-light fiber Bragg grating temperature sensor with phase-sensitive detection. *Opt. Lett.* **2018**, *43*, 3337–3340. [CrossRef]
26. Fernández-Medina, A.; Frövel, M.; López Heredero, R.; Belenguer, T.; de la Torre, A.; Moravec, C.; San Julián, R.; Gonzalo, A.; Cebollero, M.; Álvarez-Herrero, A. Embedded fiber Bragg grating sensors for monitoring temperature and thermo-elastic deformations in a carbon fiber optical bench. *Sensors* **2023**, *23*, 6499. [CrossRef]
27. Kogelnik, H. Coupled wave theory for thick hologram gratings. *Bell Syst. Tech. J.* **1969**, *48*, 2909–2947. [CrossRef]
28. Rajabzadeh, A.; Heusdens, R.; Hendriks, R.C.; Groves, R.M. Calculation of the mean strain of smooth non-uniform strain fields using conventional FBG sensors. *J. Light. Technol.* **2018**, *36*, 3716–3725. [CrossRef]
29. Lienhard, J.H.V.; Lienhard, J.H., IV. *A Heat Transfer Textbook*, 6th ed.; Phlogiston Press: Cambridge, MA, USA, 2024.
30. de Jong, S. SIMPLS: An alternative approach to partial least squares regression. *Chemom. Intell. Lab. Syst.* **1993**, *18*, 251–263. [CrossRef]
31. Negri, L.; Nied, A.; Kalinowski, H.; Paterno, A. Benchmark for peak detection algorithms in fiber Bragg grating interrogation and a new neural network for its performance improvement. *Sensors* **2011**, *11*, 3466–3482. [CrossRef]

32. Falak, P.; Lee, T.; Zahertar, S.; Shi, B.; Moog, B.; Brambilla, G.; Holmes, C.; Beresna, M. Compact high-resolution FBG strain interrogator based on laser-written 3D scattering structure in flat optical fiber. *Sci. Rep.* **2023**, *13*, 8805. [CrossRef]
33. Pustakhod, D.; Kleijn, E.; Williams, K.; Leijtens, X. High-resolution AWG-based fiber Bragg grating interrogator. *IEEE Photonics Technol. Lett.* **2016**, *28*, 2203–2206. [CrossRef]

Disclaimer/Publisher's Note: The statements, opinions and data contained in all publications are solely those of the individual author(s) and contributor(s) and not of MDPI and/or the editor(s). MDPI and/or the editor(s) disclaim responsibility for any injury to people or property resulting from any ideas, methods, instructions or products referred to in the content.